

# Tilewise Domain-Separated Selective Encryption for Remote Sensing Imagery under Chosen-Plaintext Attacks

Jilei Sun<sup>a,\*</sup>, Dianhong Wu<sup>a</sup>, Ying Su<sup>a</sup>

<sup>a</sup>*Department of Information Engineering  
Shandong University of Aeronautics  
Binzhou 256600, China*

---

## Abstract

Selective image encryption is common in remote sensing systems because it protects sensitive regions of interest (ROI) while limiting computational cost. However, many selective designs enable cross-tile structural leakage under chosen-plaintext attacks when secret-dependent transformations are reused across spatial positions. This paper proposes *Tilewise Domain-Separated Selective Encryption (TDS-SE)*, where per-tile (and optionally per-frame) keys are derived from a master secret via HKDF with explicit domain separation, and ROI masks are treated strictly as external side information.

Structural leakage is evaluated using two reconstruction-based distinguishers—a linear model and a lightweight convolutional neural network—under multiple attack settings. Experiments on RESISC45 and SEN12MS cover ablation tests, cross-position transferability, cross-sample generalization, and ROI-knowledge asymmetry.

Results show that per-tile domain separation reduces position-conditioned transfer for the linear probe, and that adding frame freshness improves robustness to imperfect ROI assumptions for the CNN probe. Cross-sample generalization exhibits mixed behavior across settings, consistent with an empirical evaluation perspective, while selective-encryption functionality is preserved under the same tiling and ROI policy. Beyond the method itself, the paper provides a structured protocol for evaluating selective encryption under realistic attacker capabilities.

*Keywords:* Selective encryption, remote sensing images, chosen-plaintext

---

\*Corresponding author.

*Email address:* sunjilei@sdua.edu.cn (Jilei Sun)

## Acknowledgments

This work was supported by the Ph.D. Scientific Research Foundation of Shandong University of Aeronautics under Grant No. 801003023049.

## 1. Introduction

Remote sensing imagery underpins civilian and defense applications such as land-use monitoring, disaster response, and infrastructure assessment. At the same time, high-resolution products may reveal sensitive content (e.g., military facilities, critical infrastructure, or privacy-relevant activity), motivating protection during onboard storage, downlink transmission, and cloud-based analytics [1, 2, 3].

Full-image encryption offers strong confidentiality but can be difficult to deploy in resource-constrained sensing pipelines due to tight compute, memory, and latency budgets. As a pragmatic alternative, selective encryption protects only a subset of visual data—typically regions of interest (ROIs), selected bit-planes, or compressed-domain components—while leaving the remainder in clear form to preserve efficiency and compatibility with downstream processing [4, 5, 6, 7].

Selective protection, however, introduces risks that are not captured by standard image-randomness metrics. Many chaos-inspired and permutation-diffusion designs report favorable entropy, correlation, NPCR, or UACI scores, yet cryptanalytic studies repeatedly show that such statistics do not imply resistance to adaptive attacks. In particular, broad classes of permutation-diffusion ciphers can be broken or partially inverted under chosen-plaintext access when structural reuse exists across encryption invocations [8, 9, 10, 11, 12, 13, 6, 14, 15].

This paper targets a failure mode that is especially relevant to selective encryption for tiled remote sensing products: structural transferability. When a system reuses identical or correlated secret-dependent transformations across tiles, positions, or frames, an adversary with chosen-plaintext capability can learn a tile-conditioned mapping on one subset of data and transfer it to other tiles or other images encrypted under the same long-term key. Such transfer may persist even when ciphertext tiles appear statistically random, because

the distinguisher exploits invariant structure rather than weak confusion in a single ciphertext instance [11, 16].

To mitigate structural reuse at the granularity where selective protection is applied, we adopt a framework-level principle: cryptographic domain separation should match the granularity of selective encryption. Domain separation is standard in modern cryptographic engineering to ensure that derived keys (or oracle domains) for different purposes are computationally independent even when they originate from the same master secret [17, 18]. We instantiate this principle as *Tilewise Domain-Separated Selective Encryption (TDS-SE)*: per-tile (and optionally per-frame) subkeys are derived from a master key using explicit domain tags that bind the derivation to tile index and context. The ROI mask is treated as external side information and is not allowed to influence secret state, avoiding circular dependencies that an adversary could exploit via chosen-plaintext manipulation.

Rather than claiming formal indistinguishability guarantees, we adopt an empirical security evaluation aligned with realistic attacker capabilities in remote sensing pipelines. We assess leakage using reconstruction-based distinguishers that attempt to learn transferable structure from chosen-plaintext queries, including a linear model and a lightweight convolutional model. This choice is motivated by evidence that learning-based methods can serve as effective distinguishers against structured cryptographic transformations, complementing classical analyses [19, 16, 20].

The main contributions are:

**TDS-SE framework.** We propose a tiled selective-encryption pipeline in which per-tile keys are derived from a master secret via explicit domain separation, instantiated using standard AES-CTR. This design suppresses cross-tile structural reuse while remaining compatible with practical selective encryption workflows.

**CPA-oriented evaluation protocol.** We introduce an empirical evaluation methodology tailored to chosen-plaintext settings, targeting cross-position transfer, cross-sample generalization, and ROI-knowledge asymmetry. This protocol complements conventional statistical reporting and directly measures structural leakage.

**Comprehensive experimental validation.** Using the public remote sensing datasets NWPU-RESISC45 and SEN12MS, we quantify how domain separation affects structural leakage and transferability, and we compare against ablation variants and representative baselines[1, 2, 21, 22, 23, 24].

## 2. Related Work

Selective and partial encryption have long been studied in multimedia security, motivated by the observation that encrypting a carefully chosen subset of the representation can provide perceptual or semantic protection at substantially lower cost. Early work explored selective encryption of JPEG2000 bitstreams and compressed-domain components, showing that encrypting a modest fraction of syntax elements can severely degrade visual quality while preserving codec compliance [4]. Subsequent schemes extended the idea to spatial-domain ROI encryption and pixel-selection strategies (e.g., pixels of interest), targeting scenarios where latency or energy budgets preclude full encryption [5, 6, 7].

**Chaos-based and permutation–diffusion image ciphers.** A large body of image-encryption work combines chaos-inspired key streams with Fridrich-style permutation–diffusion architectures [25]. Although such constructions can yield strong diffusion and visually noise-like ciphertexts, extensive cryptanalysis shows that many instances are vulnerable when identical or related transformations are reused across encryptions. Representative analyses demonstrate chosen-plaintext (and related) attacks that recover equivalent keys, expose secret permutations, or invert diffusion layers with complexity linear in image size [8, 9, 10, 12, 13, 26, 27, 28]. Recent reviews confirm that structurally similar weaknesses persist in many modern variants [14, 15]. These results motivate evaluation criteria beyond single-image statistics.

**Chosen-plaintext security and the limits of statistical metrics.** In symmetric cryptography, chosen-plaintext security is a baseline requirement, building on foundational notions of secrecy and probabilistic encryption [29, 30]. In image-encryption papers, however, evaluation still often relies on entropy, histogram uniformity, and correlation tests. Cryptanalysis of permutation–diffusion schemes using carefully designed plaintext queries repeatedly shows that high entropy does not prevent an adversary from learning reusable structure [11, 9, 6]. This gap is amplified in selective encryption, where ROI/non-ROI asymmetry can provide side information that facilitates alignment and transfer.

**Remote sensing–oriented encryption and selective protection.** Remote sensing introduces additional constraints and attacker opportunities: large data volumes, tiled products, repeated processing over long missions, and heterogeneous downstream analytics. Several works propose hybrid designs combining standard primitives (often AES modes) with chaotic components

to balance performance and perceived security for satellite imagery and remote sensing payloads [24, 21, 23, 3, 31, 32]. These studies highlight the engineering motivation for selective or lightweight protection but typically evaluate security primarily through statistics rather than adversarial learning or transfer-based analyses.

**Domain separation and key derivation.** Domain separation is a standard engineering technique to prevent unsafe key or oracle reuse across contexts by binding derived material to a labeled domain. In modern KDF practice, this is commonly realized through a context (e.g., `info`) parameter that produces independent keys for different applications even under the same input key material [17, 18]. Despite being well established in applied cryptography, explicit domain separation is rarely enforced at tile or frame granularity in selective image-encryption pipelines, where state reuse is often treated as an efficiency optimization.

**Learning-based distinguishers and empirical security evaluation.** Recent cryptanalytic work shows that machine learning can construct effective distinguishers and key-recovery pipelines by exploiting subtle, repeatable structure in reduced-round or structured ciphers [19, 16, 20]. While the threat model and primitives differ from block-cipher cryptanalysis, the broader implication is that “looks random” does not guarantee robustness against data-driven adversaries. For selective encryption, this motivates protocols that explicitly test whether an attacker can transfer learned structure across positions and samples under chosen-plaintext access.

In summary, prior literature provides (i) efficient selective-encryption mechanisms, (ii) extensive evidence that chaos-based permutation–diffusion schemes can leak under CPA when reuse exists, and (iii) principled tools—domain separation and learning-based distinguishers—that can be adapted to evaluate and mitigate structural leakage. The present work integrates these threads by enforcing tilewise domain separation in the key schedule and evaluating security through transferability-focused CPA experiments on public remote sensing benchmarks [1, 2, 3].

### 3. Threat Model and Security Objectives

This paper targets practical protection for tilewise selective encryption under chosen-plaintext capabilities. We do not claim reduction-based security; instead, we aim to reduce empirically observable structural leakage and

transferability that arise when selective pipelines reuse correlated secret-dependent transformations across tiles or frames.

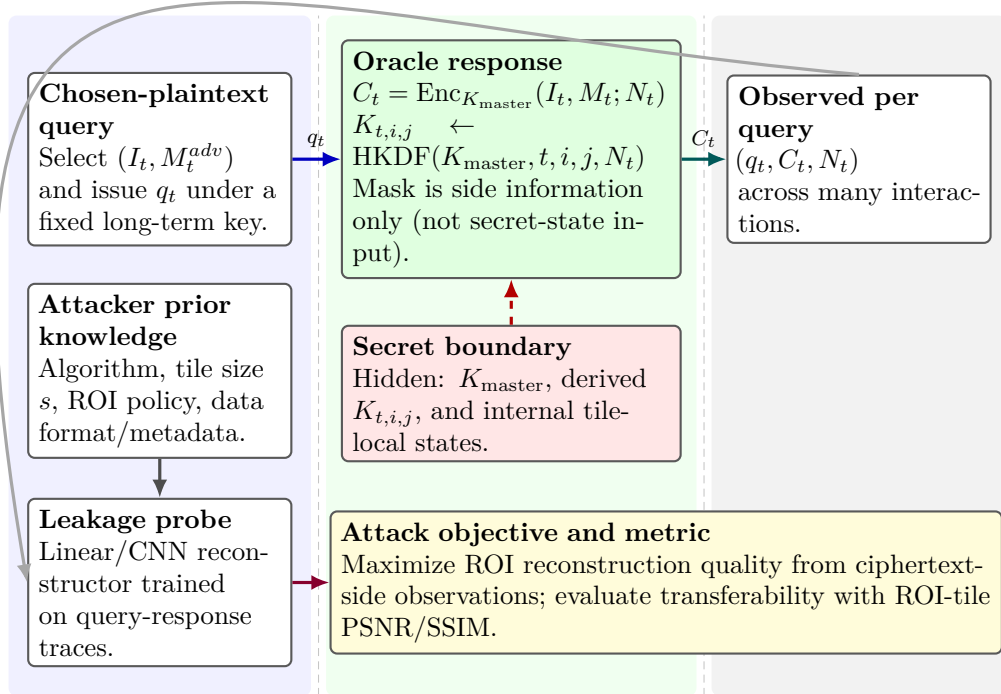


Figure 1: Chosen-plaintext (CPA) interface and information boundary for tilewise selective encryption. The attacker controls plaintext/ROI queries and observes the public transcript  $(q_t, C_t, N_t)$ , while  $K_{\text{master}}$  and derived per-tile keys remain hidden. The ROI mask is treated as external side information and does not derive secret state.

### 3.1. System and Trust Assumptions

We consider a sender that applies tilewise selective encryption to ROI tiles (e.g.,  $64 \times 64$ ) and reuses a long-term master key across many images/frames. The ROI mask is available to the sender and is treated strictly as external side information (from metadata or a precomputed detector); in particular, secret

state must not be derived from plaintext pixels. Side-channel and hardware attacks are out of scope.

### 3.2. Adversary Model

The adversary is computationally bounded and has chosen-plaintext access to an encryption oracle under a fixed long-term key. The attacker knows the algorithm, tiling scheme, and ROI handling, and may collect ciphertexts across many images/frames; in some scenarios, the attacker may also influence externally supplied ROI metadata. The attacker does not learn  $K_{\text{master}}$  or any derived subkeys.

### 3.3. Threat–Metric–Experiment Mapping

To align evaluation with the threat model, we map each risk to concrete metrics and experiments. The primary evidence is transferability-oriented performance on ROI tiles (PSNR/SSIM under reconstruction-based attacks); supplementary diagnostics are treated as secondary evidence. Table 1 summarizes the mapping.

Table 1: Mapping from threat model to evaluation metrics and experimental evidence.

<b>Threat / Risk</b>	<b>Primary Metric(s)</b>	<b>Experiment(s)</b>
Cross-tile structural reuse (transfer across positions)	ROI-tile PSNR/SSIM under fixed-position training and cross-position testing	Cross-tile transferability protocol (E5)
Cross-sample structural reuse (transfer across images)	ROI-tile PSNR/SSIM under disjoint train/test image subsets	Train on subset A, test on disjoint subset B (E3)
ROI manipulation and boundary cues	ROI-tile PSNR/SSIM under known/unknown/mismatched ROI assumptions	ROI-knowledge asymmetry protocol (E4)
Cross-frame reuse under a long-term key (secondary in this version)	Frame-conditioned ablation difference (A1 vs A3)	Indirectly examined in E2/E3; dedicated temporal-sequence evaluation is left for future work

This mapping guides the experimental design in Section 5 and ensures that each reported result corresponds to a specific leakage pathway identified in the threat model.

#### 4. Proposed Method: TDS-SE

TDS-SE is a tilewise selective-encryption pipeline that targets empirically observable transferability under the chosen-plaintext threat model (Section 3). The guiding rule is: the derivation domain must match the granularity of selective protection. Accordingly, we enforce per-tile (and optionally per-frame) domain separation via HKDF, while treating ROI masks as external side information.

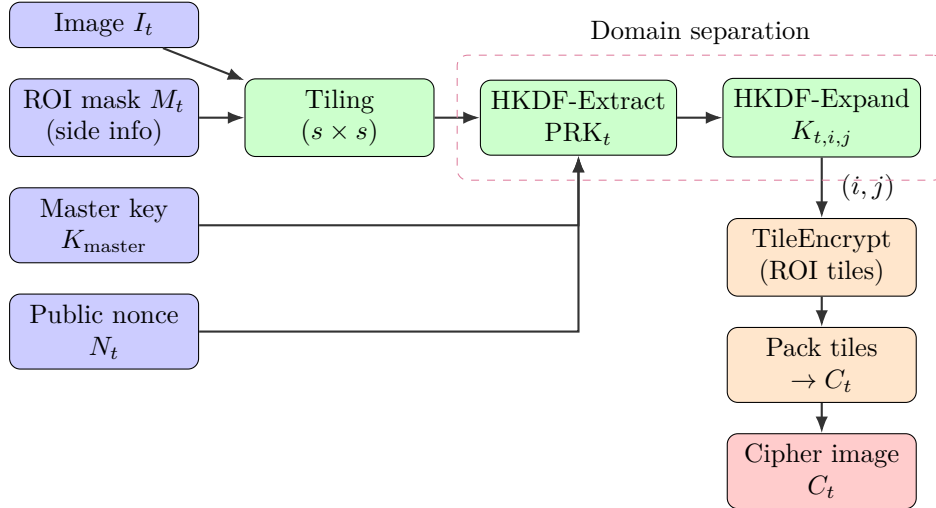


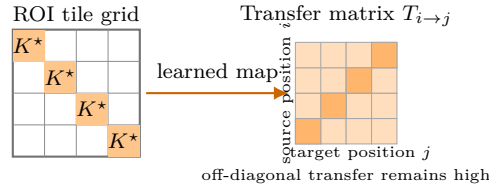
Figure 2: End-to-end architecture of TDS-SE. A fresh public nonce provides per-image freshness; HKDF derives independent per-tile keys to prevent cross-tile structural reuse.

##### 4.1. System Model and Notation

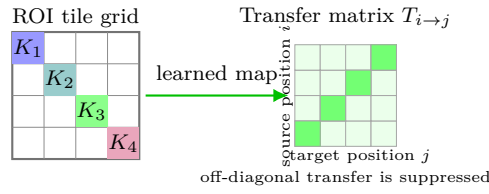
Let  $I_t$  denote an image (or frame) at time index  $t$ , and let  $M_t$  denote a binary ROI mask. The image is partitioned into non-overlapping tiles of size  $s \times s$  (e.g.,  $s = 64$ ), indexed by coordinates  $(i, j)$ . We use  $\text{ROI}(i, j) \in \{0, 1\}$  to indicate whether tile  $(i, j)$  is an ROI tile under mask  $M_t$ .

We also define the ROI tile index set as  $\Omega_{\text{ROI}}(M_t) = \{(i, j) : \text{ROI}(i, j) = 1\}$ .

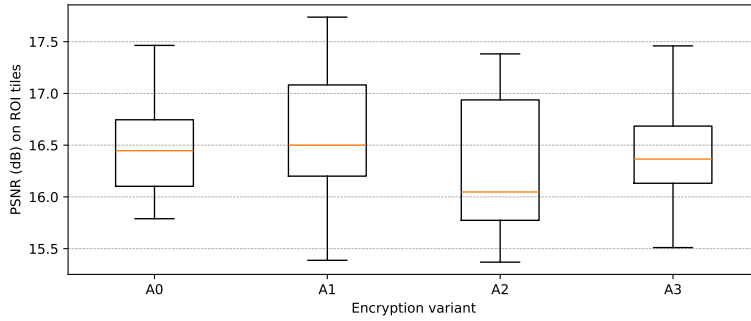
The method takes as input:



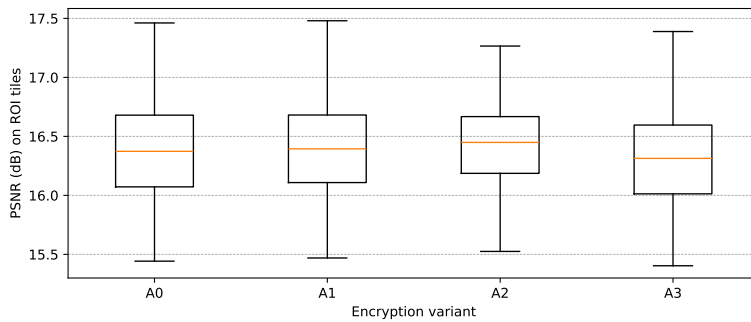
(a) Key reuse across ROI tiles (no domain separation).



(b) Per-tile key domains (tilewise separation).



(c) E5 boxplot: Att-LR, source=center.



(d) E5 boxplot: Att-CNN, source=center.

Figure 3: Mechanism-and-evidence view of cross-tile transferability. Top: key-assignment schematics and conceptual transfer matrices for a structure-reusing baseline versus tilewise domain separation. Bottom: empirical E5 boxplots (source=center) for Att-LR and Att-CNN, showing bounded transfer and variant-dependent differences.

Table 2: Comparison of structure-reusing selective encryption and the proposed tilewise domain-separated framework.

Design Property	Structure-Reusing	Proposed
Selective encryption granularity	Tile/block	Tile
Per-tile independent key	✗	✓
Per-frame nonce freshness	Optional/ad hoc	✓
Key derivation with domain separation	✗	✓ (HKDF)
Cross-tile diffusion	Enabled	Suppressed
Structural reuse across tiles	Yes	No
CPA cross-tile transferability	High	Reduced

- Secret master key  $K_{\text{master}}$ ;
- Public per-frame nonce  $N_t$  (generated fresh for each  $t$ );
- Image tiles  $\{\text{Tile}_t(i, j)\}$  and ROI indicators  $\text{ROI}(i, j)$ .

The method outputs ciphertext tiles  $\{C_t(i, j)\}$ .

**Tile and byte-sequence notation.** For a tile at position  $(i, j)$  in frame  $t$ , we write the plaintext tile as  $T_{t,i,j} \equiv \text{Tile}_t(i, j)$  and the corresponding ciphertext tile as  $C_{t,i,j}$ . When a byte-vector representation is needed, we use  $x_{t,i,j}$  and  $z_{t,i,j}$  to denote the plaintext and ciphertext byte sequences obtained by flattening  $T_{t,i,j}$  and  $C_{t,i,j}$  in a fixed order.

**Key-derivation symbols.** The master secret key is denoted by  $K_{\text{master}}$  and the public per-frame nonce by  $N_t$ . We use  $\text{PRK}_t$  for the frame-level pseudorandom key and  $K_{t,i,j}$  for the per-tile key. Throughout the paper, the public domain-separation strings are  $\text{info}_{i,j} = \text{"TILE"} \parallel \text{Encode}(i, j)$  and  $\text{info}_{t,i,j} = \text{"TILE"} \parallel \text{Encode}(t, i, j)$ . We use  $\text{info}_{i,j}$  only for the tile-only variant (A2), and  $\text{info}_{t,i,j}$  for the per-frame-and-tile variant (A3), to make the domain scope explicit. The concrete HKDF derivation equations are given in Section 4.3, and variant-specific rules are summarized in Section 4.8.

#### 4.2. Tile Partitioning and ROI Handling

We partition the image into non-overlapping tiles of fixed size  $s \times s$ . Selective encryption operates at tile granularity: a tile is encrypted if its ROI coverage exceeds a threshold (e.g.,  $\geq 50\%$  ROI pixels), and the entire tile is then protected. This quantization is an engineering choice that prioritizes isolation and repeatability of protection units.

The ROI mask is treated as external side information and is assumed public (Section 3). Crucially, we do not derive secret state from plaintext-dependent ROI extraction, to avoid plaintext-feedback vulnerabilities under chosen-plaintext access.

#### 4.3. Per-Frame Freshness and Per-Tile Domain Separation

We generate a fresh public nonce  $N_t$  for each frame/image, ensuring that derived material changes across frames even under a fixed long-term key.

For each ROI tile at position  $(i, j)$ , we derive an independent key  $K_{t,i,j}$  using HKDF. Using the notation in Section 4.1, the derivation binds both the frame context (via  $t$  and  $N_t$ ) and the tile context (via  $(i, j)$ ):

$$\begin{aligned} \text{PRK}_t &\leftarrow \text{HKDF.Extract}(N_t, K_{\text{master}}), \\ K_{t,i,j} &\leftarrow \text{HKDF.Expand}(\text{PRK}_t, \text{info}_{t,i,j}, L). \end{aligned} \tag{1}$$

Here,  $L$  is the output length (e.g., 32 bytes). The nonce  $N_t$  is public and provides freshness (not secrecy). Tile coordinates are also public; their role is to enforce distinct derivation domains per tile, preventing key reuse across spatial positions.

#### 4.4. Tile-Local Encryption Primitive

After deriving  $K_{t,i,j}$ , each ROI tile is encrypted independently. The framework does not mandate a specific cipher; instead, it enforces two structural constraints: (i) encryption state must remain strictly local to each tile (no cross-tile permutation paths, diffusion chains, or keystream dependencies), and (ii) plaintext changes within one tile must not influence ciphertext outside that tile.

**Primary instantiation (AES-CTR per tile).** To avoid ambiguity about the underlying primitive and to align with standard cryptographic practice, we instantiate `EncTile` using AES in CTR mode on the raw tile byte string. Concretely, we truncate the derived tile key to 128 bits ( $K_{t,i,j}^{(128)}$ ) and encrypt with AES-CTR using a 64-bit nonce prefix derived from the public per-frame nonce (Section 4.5); the counter starts at zero and advances within the tile. Because  $K_{t,i,j}$  is domain-separated, keystream reuse across tiles can only occur when the derivation rule intentionally omits domain separation (variants A0/A1).

**Alternative instantiation (ablation).** For completeness and to isolate the effect of domain separation from any particular block-cipher choice, we

also provide a lightweight tile-local stream–permute–diffuse instantiation as an ablation (Appendix [Appendix A](#)). This alternative is not required by the framework; it is included only to demonstrate that the key-derivation discipline, rather than a specific cipher, drives the transferability behaviour.

#### 4.5. End-to-End Selective Encryption Procedure

The end-to-end workflow is as follows. For each image/frame, we generate a fresh public nonce to provide per-frame freshness. The image is partitioned into non-overlapping tiles and each tile is labeled by the ROI mask. For ROI tiles, we derive a per-tile key via HKDF with domain separation that embeds the frame nonce and tile coordinates, then apply the tile-local primitive. Non-ROI tiles pass through unchanged to preserve efficiency and downstream usability. Algorithm 1 summarizes the procedure.

We enforce strict tile locality (no cross-tile state) and derive cryptographic state solely from  $K_{\text{master}}$ , the public nonce, and the tile index. The ciphertext image is reconstructed by merging encrypted and unencrypted tiles, accompanied by the public nonce.

Algorithm 1 illustrates the full domain-separated instantiation (A3); A0–A2 differ only in the key-derivation rule as defined in Section 4.8, while the tile-local primitive remains unchanged.

#### 4.6. Instantiation and Reproducibility Parameters

We summarize the concrete parameterization used by the reference implementation to ensure reproducibility.

**HKDF.** We use HKDF-Extract and HKDF-Expand with HMAC-SHA256. The per-frame public nonce  $N_t$  is 16 bytes. For variant A2 (tile-only),  $N_t$  is fixed to  $\mathbf{0}^{16}$  to isolate the effect of tile-coordinate binding; for the other variants,  $N_t$  is sampled uniformly at random per image/frame. The HKDF output length is  $L = 32$  bytes, yielding a tile key  $K_{t,i,j} \in \{0, 1\}^{256}$ .

**Domain-separation tag.** The HKDF `info` field is ASCII "TILE" optionally concatenated with the 16-bit big-endian tile indices  $(i, j)$ :

$$\text{info}_{t,i,j} = \text{"TILE"} \parallel i_{\langle 2 \rangle} \parallel j_{\langle 2 \rangle},$$

where  $i_{\langle 2 \rangle}$  denotes a two-byte big-endian encoding. Variants A0/A1 omit the coordinate suffix by construction.

**AES-CTR tile encryption.** For the AES-CTR instantiation, we use the first 16 bytes of  $K_{t,i,j}$  as the AES-128 key and the first 8 bytes of  $N_t$

---

**Algorithm 1** End-to-end tilewise selective encryption (shown for A3: per-frame and per-tile domain separation)

---

```

1: Input:  $K_{\text{master}}$ , image/frame  $I_t$ , ROI mask  $M_t$ 
2: Generate fresh public nonce  $N_t$ 
3: Partition  $I_t$  into tiles  $\{\text{Tile}_t(i, j)\}$  of size  $s \times s$ 
4:                                     // HKDF-Extract(salt= $N_t$ , input key= $K_{\text{master}}$ )
5:  $\text{PRK}_t \leftarrow \text{HKDF.Extract}(N_t, K_{\text{master}})$ 
6: for each tile  $(i, j)$  do
7:    $\mathbf{x}_{t,i,j} \leftarrow \text{Tile}_t(i, j)$  // Plaintext tile bytes
8:   if  $(i, j) \in \Omega_{\text{ROI}}(M_t)$  then
9:      $\text{info}_{t,i,j} \leftarrow \text{"TILE"} \parallel \text{Encode}(t, i, j)$  // Domain-separation tag
10:     $K_{t,i,j} \leftarrow \text{HKDF.Expand}(\text{PRK}_t, \text{info}_{t,i,j}, L)$  // L bytes
11:     $\mathbf{z}_{t,i,j} \leftarrow \text{EncTile}(K_{t,i,j}, \mathbf{x}_{t,i,j})$ 
12:   else
13:      $\mathbf{z}_{t,i,j} \leftarrow \mathbf{x}_{t,i,j}$ 
14:   end if
15: end for
16: Merge  $\{\mathbf{z}_{t,i,j}\}$  to form ciphertext image  $C_t$ 
17: Output:  $(C_t, N_t)$ 

```

---

as a 64-bit nonce prefix. CTR uses a 64-bit counter initialized to zero and incremented for successive blocks within the tile; encryption is applied to the byte string of the ROI tile, and the output is reshaped back to the tile tensor. This construction preserves strict tile locality: there is no chaining across tiles, and counters do not cross tile boundaries.

#### 4.7. Design Rationale

These design choices follow directly from the transferability-oriented threat model.

**Per-tile domain separation:** binding derivation to  $(i, j)$  prevents learning at one position from transferring to other positions under the same long-term key.

**Per-frame freshness:** introducing a public nonce  $N_t$  ensures derived tile keys differ across images/frames, limiting accumulation of reusable structure over time.

**Tile-local state isolation:** diffusion and any permutation are reset at tile boundaries, so any observed transfer must come from key/domain reuse rather than cross-tile state spillover.

Plaintext-dependent state derivation is intentionally avoided to prevent adaptive distinguishability under chosen-plaintext probing.

#### 4.8. Variant Definitions

**Encryption variants.** All variants share the same tiling structure and ROI selection rule; they differ only in the scope at which domain separation is applied in the key-derivation process. Table 3 summarizes the four selective-encryption variants used in the experiments.

Table 3: Summary of encryption variants

ID	Definition (key-derivation rule and domain-separation scope)
A0	<b>none:</b> $K_{t,i,j} = K_{\text{master}}$ ; no per-frame freshness; no per-tile separation
A1	<b>frame-only:</b> $K_{t,i,j} = \text{PRK}_t$ ; per-frame freshness only (shared across tiles)
A2	<b>tile-only:</b> $K_{t,i,j} = \text{HKDF}.\text{Expand}(\text{PRK}_0, \text{info}_{i,j}, L)$ ; per-tile separation only (no frame nonce)
A3	<b>full separation:</b> $K_{t,i,j} = \text{HKDF}.\text{Expand}(\text{PRK}_t, \text{info}_{t,i,j}, L)$ ; per-frame freshness + per-tile separation

where  $\text{PRK}_0 = \text{HKDF.Extract}(0, K_{\text{master}})$ .

A classical non-selective baseline, denoted by **AES-CTR**, encrypts the entire image without ROI restriction.

For a reviewer-requested CPA sanity check (Section 5.9), we also define an intentionally insecure reuse baseline **B1\_no\_ds** that removes domain separation entirely: all ROI tiles within a frame share the same derived key/keystream parameters. This baseline is used only to demonstrate breakability under chosen plaintext; it is not part of TDS-SE.

## 5. Experiments and Results

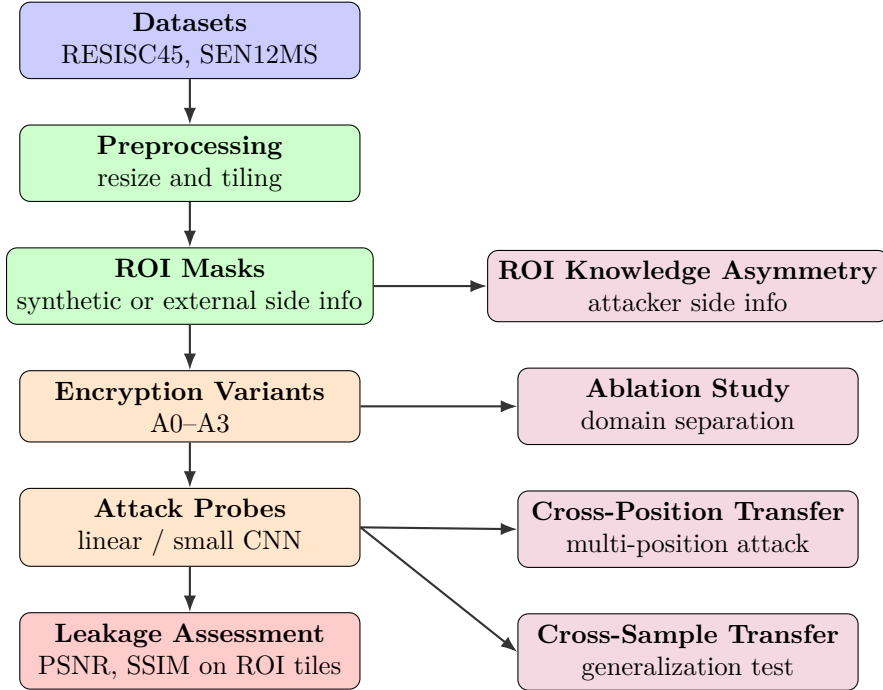


Figure 4: Experimental evaluation protocol under chosen-plaintext access. E2–E5 refer to the scenario definitions summarized in Table 4 (see Section 5 for results).

We evaluate TDS-SE under chosen-plaintext access using scenarios that isolate ablation effects, cross-position transfer, cross-sample generalization, and ROI-knowledge asymmetry.

**Evaluation protocols.** We reference scenarios by identifiers **E2–E5** (E1 is an internal correctness sanity check and is omitted). Table 4 defines E2–E5; Fig. 4 visualizes the workflow.

Table 4: Summary of evaluation scenarios.

ID	Definition (attacker probe and split)
E2	<b>Ablation:</b> compare A0–A3 under the same dataset and ROI setting to isolate the effect of per-frame nonce and per-tile domain separation.
E3	<b>Cross-sample transferability:</b> train attacker on ROI tiles from image subset A and test on disjoint subset B (50/50 split).
E4	<b>ROI-knowledge asymmetry:</b> compare attacker performance when the ROI mask is known vs unknown to the attacker at inference time.
E5	<b>Cross-tile transferability:</b> train attacker on ROI tiles from one tile position and test on different positions within the same image/frame.

For consistency across E2–E5, we report ROI-tile PSNR (dB) and SSIM as primary leakage indicators in all main tables and figures. Higher values indicate stronger attacker reconstruction ability, whereas lower values indicate weaker recoverability.

### 5.1. Datasets and Experimental Setup

We run experiments on public remote sensing imagery. All inputs are resized to a common resolution and partitioned into non-overlapping  $64 \times 64$  tiles. ROI masks are generated synthetically to achieve a target coverage of approximately 30% and are treated as external side information. Unless stated otherwise, attacker training/testing uses a deterministic 50/50 split over image samples. We report ROI-tile PSNR (dB) and SSIM as leakage indicators (higher implies stronger reconstruction).

### 5.2. Attacker Models and Metrics

To probe structural leakage, we use two reconstruction-based distinguishers. The first is linear ridge regression on low-frequency representations obtained by downsampling ROI tiles to  $16 \times 16$  grayscale; it captures coarse dependencies while remaining interpretable. The second is a lightweight convolutional neural network trained to reconstruct the same low-frequency target, providing modest nonlinear capacity without excessive complexity. In tables, we denote them as **Att-LR** and **Att-CNN**.

We evaluate reconstruction quality on ROI tiles using PSNR (dB) and SSIM. Higher PSNR/SSIM implies stronger attacker recovery; lower values indicate reduced recoverability. Neural models are trained for ten epochs using Adam with learning rate  $10^{-3}$ . Results are averaged over test tiles, and standard deviations are reported where appropriate.

### 5.3. Ablation of Domain Separation Components

We compare A0–A3 to isolate the contributions of per-frame freshness and per-tile domain separation. Table 5 summarizes the results. Overall, domain separation primarily affects transferability rather than the mean PSNR/SSIM: per-tile separation tends to reduce position-conditioned transfer under the linear probe, whereas adding frame freshness improves robustness to imperfect ROI assumptions under the CNN probe.

Table 5: Ablation study (E2): impact of domain separation components on transferability-based leakage. Attackers predict low-frequency plaintext ( $16 \times 16$  grayscale) from ciphertext ROI tiles.

Dataset	Method	PSNR (dB) $\uparrow$	SSIM $\uparrow$
<i>RESISC45</i> (Att-LR)			
	A0	16.49 $\pm$ 3.99	0.197 $\pm$ 0.150
	A1	16.58 $\pm$ 4.07	0.197 $\pm$ 0.151
	A2	16.23 $\pm$ 3.91	0.188 $\pm$ 0.147
	A3	16.47 $\pm$ 4.01	0.196 $\pm$ 0.146
<i>RESISC45</i> (Att-CNN)			
	A0	16.54 $\pm$ 4.04	0.239 $\pm$ 0.190
	A1	16.51 $\pm$ 3.94	0.228 $\pm$ 0.177
	A2	16.30 $\pm$ 3.95	0.237 $\pm$ 0.188
	A3	16.35 $\pm$ 3.97	0.239 $\pm$ 0.189
<i>SEN12MS</i> (Att-LR)			
	A0	30.15 $\pm$ 5.30	0.732 $\pm$ 0.194
	A1	30.18 $\pm$ 5.15	0.734 $\pm$ 0.193
	A2	24.69 $\pm$ 3.01	0.594 $\pm$ 0.120
	A3	29.62 $\pm$ 5.15	0.726 $\pm$ 0.189
<i>SEN12MS</i> (Att-CNN)			
	A0	20.36 $\pm$ 3.24	0.016 $\pm$ 0.012
	A1	20.40 $\pm$ 3.26	0.019 $\pm$ 0.014
	A2	20.47 $\pm$ 3.28	0.024 $\pm$ 0.016
	A3	20.40 $\pm$ 3.26	0.019 $\pm$ 0.014

#### 5.4. Cross-Tile Transferability

To assess structural reuse across spatial positions, we train attackers on ROI tiles from a fixed source position and evaluate on tiles at other positions. Table 6 reports transferability metrics across source positions.

Table 6: Cross-tile transferability (E5): attacker trained on ROI tiles at one source position and evaluated across multiple target positions. Results are aggregated over target positions (mean $\pm$ std).

Attacker	Source	Method	PSNR (dB) $\uparrow$	SSIM $\uparrow$
Att-LR	center	A0	16.50 $\pm$ 0.51	0.197 $\pm$ 0.018
Att-LR	center	A1	16.61 $\pm$ 0.66	0.197 $\pm$ 0.018
Att-LR	center	A2	16.27 $\pm$ 0.68	0.188 $\pm$ 0.018
Att-LR	center	A3	16.47 $\pm$ 0.55	0.196 $\pm$ 0.015
Att-LR	corner00	A0	16.71 $\pm$ 0.56	0.213 $\pm$ 0.019
Att-LR	corner00	A1	16.80 $\pm$ 0.57	0.213 $\pm$ 0.022
Att-LR	corner00	A2	16.00 $\pm$ 0.63	0.199 $\pm$ 0.021
Att-LR	corner00	A3	16.87 $\pm$ 0.62	0.211 $\pm$ 0.018
Att-CNN	center	A0	16.44 $\pm$ 0.59	0.240 $\pm$ 0.022
Att-CNN	center	A1	16.46 $\pm$ 0.59	0.239 $\pm$ 0.022
Att-CNN	center	A2	16.52 $\pm$ 0.57	0.231 $\pm$ 0.021
Att-CNN	center	A3	16.37 $\pm$ 0.58	0.236 $\pm$ 0.022
Att-CNN	corner00	A0	16.68 $\pm$ 0.55	0.233 $\pm$ 0.021
Att-CNN	corner00	A1	16.58 $\pm$ 0.54	0.230 $\pm$ 0.021
Att-CNN	corner00	A2	16.60 $\pm$ 0.55	0.233 $\pm$ 0.021
Att-CNN	corner00	A3	16.75 $\pm$ 0.53	0.228 $\pm$ 0.021

Across both center-source and corner-source settings, transfer remains bounded. For the linear probe, the tilewise-separated variant (A2) achieves the lowest average reconstruction, supporting the claim that per-tile key separation reduces position-conditioned transfer. For the CNN probe, differences among variants are smaller in this setting; we therefore interpret the results as evidence of limited (rather than eliminated) transferability.

#### 5.5. Cross-Sample Generalization

We next test whether reconstruction models trained on one subset of images generalize to unseen images. Table 7 reports cross-sample generalization metrics.

Cross-sample behavior is mixed across attacker types and settings; accordingly, we do not claim a consistent improvement in cross-sample resistance.

Table 7: Cross-sample transferability (E3): attacker trained on ROI tiles from image subset A and evaluated on disjoint subset B (50/50 split).

Attacker	Method	PSNR (dB) $\uparrow$	SSIM $\uparrow$
Att-LR	A0	16.31 $\pm$ 4.27	0.159 $\pm$ 0.125
Att-LR	A1	16.16 $\pm$ 4.14	0.155 $\pm$ 0.125
Att-LR	A2	16.58 $\pm$ 4.38	0.170 $\pm$ 0.144
Att-LR	A3	16.16 $\pm$ 4.25	0.158 $\pm$ 0.127
Att-LR	AES-CTR	18.62 $\pm$ 3.79	0.217 $\pm$ 0.151
Att-CNN	A0	16.74 $\pm$ 4.83	0.217 $\pm$ 0.173
Att-CNN	A1	16.90 $\pm$ 4.64	0.226 $\pm$ 0.180
Att-CNN	A2	16.43 $\pm$ 4.04	0.223 $\pm$ 0.177
Att-CNN	A3	16.78 $\pm$ 4.49	0.219 $\pm$ 0.174
Att-CNN	AES-CTR	16.85 $\pm$ 4.60	0.223 $\pm$ 0.178

### 5.6. ROI Knowledge Asymmetry

We evaluate sensitivity to ROI knowledge under three conditions (known ROI, unknown ROI, and mismatched ROI). Table 8 summarizes the results. As expected, reconstruction is strongest when the ROI is known. Notably, the fully domain-separated configuration shows smaller performance variation across conditions under the CNN probe, indicating improved robustness to imperfect ROI assumptions.

### 5.7. Qualitative Visualization

Representative qualitative examples are provided in Figure 5.

Ciphertext images exhibit visually incoherent ROI regions while preserving non-ROI content, consistent with selective-encryption objectives.

### 5.8. AES-CTR Tile-Cipher Instantiation (Sanity Check)

In addition to the lightweight stream-permute-diffuse ablation (Appendix A), we implement a standard instantiation that applies AES in CTR mode to ROI tiles only (same tiling and ROI masks; counters advance deterministically within each tile to avoid keystream overlap). Table 9 summarizes the AES-CTR instantiation across protocols when available. In the provided experimental artifact, AES-CTR metrics are available for the cross-sample protocol (E3) under the Att-LR reconstructor and are comparable to A0/A3, which is consistent with the interpretation that the observed transferability trends are driven primarily by the domain-separation rule rather than by idiosyncrasies of a particular in-tile primitive.

Table 8: ROI knowledge asymmetry (E4): attacker performance when ROI is known (S1), unknown (S2), or mismatched (S3). Metrics are computed on true ROI tiles only.

Attacker	Method	Scenario	PSNR (dB) $\uparrow$	SSIM $\uparrow$
Att-LR	A0	S1_roi_known	16.31 $\pm$ 4.27	0.159 $\pm$ 0.125
Att-LR	A0	S2_roi_unknown	14.95 $\pm$ 5.10	0.169 $\pm$ 0.136
Att-LR	A0	S3_roi_wrong	16.47 $\pm$ 4.25	0.171 $\pm$ 0.133
Att-LR	A1	S1_roi_known	16.16 $\pm$ 4.14	0.155 $\pm$ 0.125
Att-LR	A1	S2_roi_unknown	15.30 $\pm$ 5.24	0.172 $\pm$ 0.141
Att-LR	A1	S3_roi_wrong	16.37 $\pm$ 4.24	0.168 $\pm$ 0.127
Att-LR	A2	S1_roi_known	16.58 $\pm$ 4.38	0.170 $\pm$ 0.144
Att-LR	A2	S2_roi_unknown	15.12 $\pm$ 5.47	0.179 $\pm$ 0.158
Att-LR	A2	S3_roi_wrong	16.67 $\pm$ 4.38	0.176 $\pm$ 0.143
Att-LR	A3	S1_roi_known	16.16 $\pm$ 4.25	0.158 $\pm$ 0.127
Att-LR	A3	S2_roi_unknown	14.98 $\pm$ 5.26	0.172 $\pm$ 0.144
Att-LR	A3	S3_roi_wrong	16.26 $\pm$ 4.25	0.174 $\pm$ 0.135
Att-CNN	A0	S1_roi_known	16.86 $\pm$ 4.76	0.221 $\pm$ 0.176
Att-CNN	A0	S2_roi_unknown	15.98 $\pm$ 4.46	0.129 $\pm$ 0.117
Att-CNN	A0	S3_roi_wrong	16.88 $\pm$ 4.65	0.223 $\pm$ 0.178
Att-CNN	A1	S1_roi_known	16.78 $\pm$ 4.82	0.218 $\pm$ 0.174
Att-CNN	A1	S2_roi_unknown	14.88 $\pm$ 4.70	0.138 $\pm$ 0.115
Att-CNN	A1	S3_roi_wrong	16.85 $\pm$ 4.53	0.224 $\pm$ 0.178
Att-CNN	A2	S1_roi_known	16.67 $\pm$ 4.25	0.220 $\pm$ 0.174
Att-CNN	A2	S2_roi_unknown	14.94 $\pm$ 4.94	0.179 $\pm$ 0.148
Att-CNN	A2	S3_roi_wrong	16.77 $\pm$ 4.64	0.216 $\pm$ 0.171
Att-CNN	A3	S1_roi_known	16.64 $\pm$ 4.22	0.231 $\pm$ 0.184
Att-CNN	A3	S2_roi_unknown	16.50 $\pm$ 4.41	0.145 $\pm$ 0.119
Att-CNN	A3	S3_roi_wrong	16.87 $\pm$ 4.56	0.226 $\pm$ 0.179

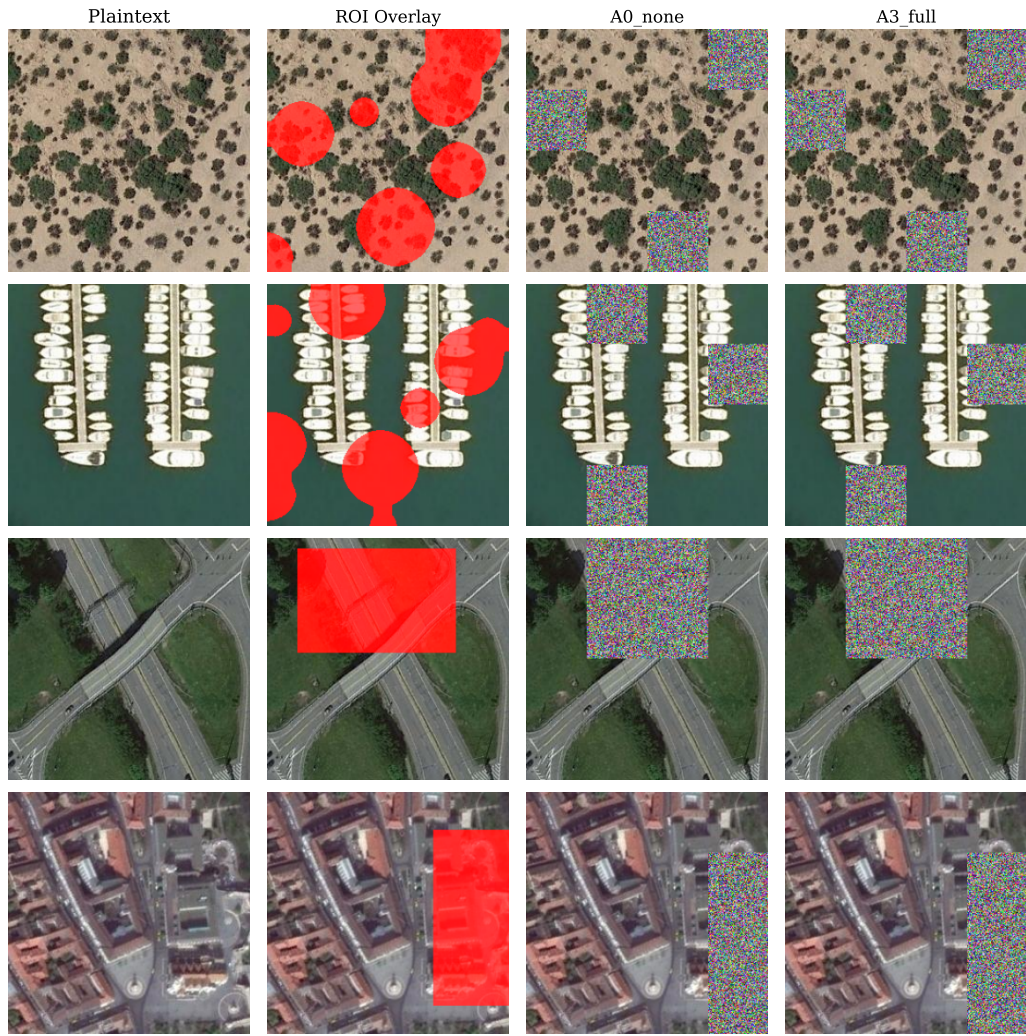


Figure 5: Qualitative examples showing plaintext, ROI mask, and ciphertext appearance for representative variants.

### 5.9. CPA Sanity Break on the Key-Reuse Baseline

Reviewers correctly noted that an empirical transfer study should also demonstrate that insecure key-reuse baselines are breakable under chosen plaintext. We therefore include a minimal CPA sanity test targeting the “no domain separation” baseline (B1), where all ROI tiles in a frame share the same derived tile key and nonce prefix.

The attacker issues a single chosen-plaintext query in which one ROI tile is set to all zeros. For CTR-mode tile encryption, the resulting ciphertext tile directly reveals the keystream. If the same keystream is reused across ROI tiles (B1), XORing this recovered keystream with another ROI ciphertext tile decrypts that tile. Under full tilewise domain separation (A3), the recovered keystream does not transfer across tiles.

Table 10 reports this sanity break on synthetic images (reported on the same  $16 \times 16$  grayscale proxy used throughout), showing near-perfect recovery for B1 and failure for A3. This supports the claim that key/keystream reuse across tiles is a first-order leakage channel and motivates the tilewise domain-separation rule.

## 6. Discussion and Limitations

### 6.1. Interpreting the Empirical Behaviour

The results exhibit a more nuanced pattern than a simple “more separation is always better” narrative. Across both datasets, domain separation does not substantially reduce average reconstruction metrics, yet it consistently stabilizes behavior across spatial positions and attacker-knowledge settings. This suggests that tilewise domain separation primarily suppresses transferable structure rather than aggressively scrambling all statistics.

In the cross-tile experiments, when a reconstruction model is trained at a fixed spatial position, its performance does not reliably transfer to other positions once per-tile separation is enforced (most clearly under the linear probe). This contrasts with structure-reusing designs, where spatial alignment can induce implicit coupling across tiles. The reduction in position-conditioned generalization supports the hypothesis that key reuse—rather than insufficient randomness—is a dominant leakage channel in selective pipelines.

Cross-sample experiments reinforce this interpretation. Although mean PSNR remains moderate across configurations, generalization from one subset of scenes to another is limited. This indicates that encryption disrupts scene-specific statistical structure more effectively than position-specific structure.

In other words, domain separation appears to constrain systematic reuse more than it eliminates all exploitable correlations.

### 6.2. Security Perspective and Scope

This study adopts an empirical distinguishability perspective rather than providing a reduction-based cryptographic proof. The goal is to assess whether structural reuse under chosen-plaintext access produces learnable and transferable patterns in realistic remote-sensing pipelines.

The results indicate that enforcing domain separation at the same granularity as selective protection reduces the most interpretable leakage vector: cross-position structural reuse. However, domain separation alone does not guarantee indistinguishability, nor does it eliminate all statistical dependence. Because selective encryption preserves portions of the image by design, complete information-theoretic concealment is outside the scope of this work.

Using AES-CTR as the reference tile cipher suggests that the proposed framework does not introduce additional leakage relative to standard block-cipher practice; the alternative stream-permute-diffuse instantiation yields comparable trends (Appendix [Appendix A](#)). Instead, it offers a principled mechanism to control key reuse in engineering contexts where tilewise protection is required.

### 6.3. Limitations

Several limitations remain.

First, the attacker objective reconstructs a low-frequency  $16 \times 16$  grayscale proxy. This captures coarse structural leakage that is relevant in remote sensing, but it does not measure higher-order semantic inference. Stronger multi-scale or transformer-based distinguishers may expose subtler dependencies [20].

Second, the CNN architecture is intentionally lightweight. This enables controlled and reproducible experiments but may underestimate a highly optimized adversary. Evaluating stronger neural distinguishers would provide a tighter upper bound on practical leakage [16, 20].

Third, ROI masks are synthetically generated at a fixed rate. Operational masks may exhibit spatial clustering, temporal consistency, or mission-driven biases. Such structure could interact with tile boundaries and alter leakage dynamics.

Finally, the framework does not provide a formal reduction to established cryptographic notions. The results demonstrate reduced empirical transferability under the tested settings, but they do not constitute a proof of indistinguishability under adaptive attacks.

#### *6.4. Future Directions*

Several extensions follow naturally. Developing a theoretical model that quantifies how domain-separated derivation constrains transferability would help bridge empirical observations and formal reasoning. Integrating authenticated encryption could strengthen end-to-end security for deployment scenarios. Finally, studying adaptive ROI generation under strict side-information constraints would clarify how content-aware selection interacts with domain-separated protection.

## **7. Conclusion**

This paper presented TDS-SE, a selective-encryption framework that targets structural transferability under chosen-plaintext access. By enforcing per-tile and per-frame domain separation and adopting a protocol-driven evaluation methodology, the approach addresses a key-reuse vulnerability widely discussed in selective-encryption pipelines. Experiments on public remote sensing datasets provide empirical evidence that TDS-SE can suppress position-conditioned transfer under the linear probe and improve robustness to ROI-knowledge mismatch under the CNN probe. These effects are setting-dependent, motivating protocol-based evaluation rather than reliance on a single aggregate metric.

## **Appendix A. Alternative Tile-Local Primitive (Ablation)**

To demonstrate that the observed transferability effects are driven by the key-derivation discipline rather than by a specific block cipher, we provide a lightweight tile-local stream-permute-diffuse instantiation as an ablation. This primitive is strictly local to each tile and resets all state at tile boundaries.

---

**Algorithm 2** Alternative tile-local stream-permute-diffuse primitive (ablation)

---

```

1: Input: per-tile key  $K_{t,i,j}$ , tile bytes  $\mathbf{x}$ 
2:  $\mathcal{S}_1 \leftarrow \text{PRF\_Expand}(K_{t,i,j} \parallel 0x01, |\mathbf{x}|)$            // Confusion keystream
3:  $\mathcal{S}_2 \leftarrow \text{PRF\_Expand}(K_{t,i,j} \parallel 0x02, |\mathbf{x}|)$            // Diffusion keystream
4:  $\mathbf{y} \leftarrow \mathbf{x} \oplus \mathcal{S}_1$                                            // Stream masking
5: if Permutation enabled then
6:    $\pi \leftarrow \text{PermIndex}(\mathcal{S}_1, |\mathbf{y}|)$                        // Per-tile Fisher-Yates from  $\mathcal{S}_1$ 
7:    $\mathbf{y} \leftarrow \mathbf{y}[\pi]$                                        // Reorder within tile only
8: end if
9:                                           // Tile-local diffusion: chain resets at tile boundary
10:  $\mathbf{z}[0] \leftarrow \mathbf{y}[0] \oplus \mathcal{S}_2[0]$ 
11: for  $k = 1$  to  $|\mathbf{y}| - 1$  do
12:    $\mathbf{z}[k] \leftarrow \mathbf{y}[k] \oplus \mathbf{z}[k - 1] \oplus \mathcal{S}_2[k]$ 
13: end for
14: Output: ciphertext tile bytes  $\mathbf{z}$ 

```

---

Table 9: AES-CTR tile-cipher instantiation reported across evaluation protocols when available. Entries are extracted from the corresponding protocol CSVs. Missing entries (-) indicate that the protocol was not regenerated with `B_AES_CTR` enabled.

Protocol	Dataset	Attacker	PSNR (dB) $\uparrow$	SSIM $\uparrow$
E3 (Cross-sample)	RESISC45	Att-LR	18.62 $\pm$ 3.79	0.217 $\pm$ 0.151
E3 (Cross-sample)	SEN12MS	Att-LR	32.78 $\pm$ 5.77	0.775 $\pm$ 0.191
E5 (Cross-tile)	SEN12MS	Att-LR	27.72 $\pm$ 3.58	0.698 $\pm$ 0.166
E5 (Cross-tile)	SEN12MS	Att-LR	24.15 $\pm$ 3.55	0.615 $\pm$ 0.127
E5 (Cross-tile)	SEN12MS	Att-LR	28.29 $\pm$ 3.82	0.716 $\pm$ 0.165
E5 (Cross-tile)	SEN12MS	Att-LR	24.31 $\pm$ 3.45	0.646 $\pm$ 0.135
E5 (Cross-tile)	SEN12MS	Att-LR	26.23 $\pm$ 3.39	0.711 $\pm$ 0.137
E5 (Cross-tile)	SEN12MS	Att-LR	28.38 $\pm$ 3.51	0.714 $\pm$ 0.163
E5 (Cross-tile)	SEN12MS	Att-LR	26.89 $\pm$ 3.49	0.673 $\pm$ 0.147
E5 (Cross-tile)	SEN12MS	Att-LR	26.43 $\pm$ 3.23	0.656 $\pm$ 0.165
E5 (Cross-tile)	SEN12MS	Att-LR	27.08 $\pm$ 3.52	0.714 $\pm$ 0.120
E5 (Cross-tile)	SEN12MS	Att-LR	26.16 $\pm$ 3.31	0.670 $\pm$ 0.162
E5 (Cross-tile)	SEN12MS	Att-LR	27.79 $\pm$ 3.74	0.713 $\pm$ 0.167
E5 (Cross-tile)	SEN12MS	Att-LR	28.21 $\pm$ 3.83	0.700 $\pm$ 0.163
E5 (Cross-tile)	SEN12MS	Att-LR	25.89 $\pm$ 3.13	0.674 $\pm$ 0.153
E5 (Cross-tile)	SEN12MS	Att-LR	26.98 $\pm$ 3.35	0.691 $\pm$ 0.162
E5 (Cross-tile)	SEN12MS	Att-LR	23.46 $\pm$ 2.86	0.620 $\pm$ 0.106
E5 (Cross-tile)	SEN12MS	Att-LR	26.82 $\pm$ 3.46	0.669 $\pm$ 0.146
E5 (Cross-tile)	SEN12MS	Att-LR	28.08 $\pm$ 3.74	0.710 $\pm$ 0.159
E5 (Cross-tile)	SEN12MS	Att-LR	25.75 $\pm$ 3.48	0.663 $\pm$ 0.145
E5 (Cross-tile)	SEN12MS	Att-LR	25.57 $\pm$ 3.31	0.682 $\pm$ 0.128
E5 (Cross-tile)	SEN12MS	Att-LR	25.63 $\pm$ 3.31	0.653 $\pm$ 0.131
E5 (Cross-tile)	SEN12MS	Att-LR	26.31 $\pm$ 3.37	0.656 $\pm$ 0.137
E5 (Cross-tile)	SEN12MS	Att-LR	25.65 $\pm$ 3.16	0.620 $\pm$ 0.149
E5 (Cross-tile)	SEN12MS	Att-LR	27.59 $\pm$ 3.57	0.717 $\pm$ 0.121
E5 (Cross-tile)	SEN12MS	Att-LR	25.70 $\pm$ 3.29	0.660 $\pm$ 0.153
E5 (Cross-tile)	SEN12MS	Att-LR	26.62 $\pm$ 3.13	0.700 $\pm$ 0.127
E5 (Cross-tile)	SEN12MS	Att-LR	27.66 $\pm$ 3.78	0.708 $\pm$ 0.165
E5 (Cross-tile)	SEN12MS	Att-LR	28.21 $\pm$ 3.72	0.688 $\pm$ 0.163
E5 (Cross-tile)	SEN12MS	Att-LR	27.70 $\pm$ 3.40	0.705 $\pm$ 0.168
E5 (Cross-tile)	SEN12MS	Att-LR	26.61 $\pm$ 3.06	0.683 $\pm$ 0.156
E5 (Cross-tile)	SEN12MS	Att-LR	27.18 $\pm$ 2.91	0.699 $\pm$ 0.140

Table 10: CPA sanity break on the key-reuse baseline (synthetic images). A single chosen-plaintext query on one ROI tile recovers the keystream; the recovered keystream decrypts other ROI tiles only when tilewise domain separation is absent. Metrics are reported on the  $16 \times 16$  grayscale proxy used throughout the paper.

Method	PSNR $\uparrow$	SSIM $\uparrow$
B1	$99.00 \pm 0.00$	$1.000 \pm 0.000$
A3	$23.32 \pm 0.35$	$0.167 \pm 0.066$

## References

- [1] G. Cheng, J. Han, X. Lu, Remote sensing image scene classification: Benchmark and state of the art, *Proceedings of the IEEE* 105 (10) (2017) 1865–1883. doi:[10.1109/JPROC.2017.2675998](https://doi.org/10.1109/JPROC.2017.2675998).
- [2] M. Schmitt, L. H. Hughes, C. Qiu, X. X. Zhu, SEN12MS – a curated dataset of georeferenced multi-spectral sentinel-1/2 imagery for deep learning and data fusion, in: *ISPRS Annals of the Photogrammetry, Remote Sensing and Spatial Information Sciences*, Vol. IV-2/W7, 2019, pp. 153–160. doi:[10.5194/isprs-annals-IV-2-W7-153-2019](https://doi.org/10.5194/isprs-annals-IV-2-W7-153-2019).
- [3] P. Luo, J. Liu, J. Xu, Q. Dang, D. Mu, Remote sensing images secure distribution scheme based on deep information hiding, *Remote Sensing* 16 (8) (2024) 1331. doi:[10.3390/rs16081331](https://doi.org/10.3390/rs16081331).
- [4] R. Norcen, M. Podesser, A. Pommer, A. Uhl, Selective encryption of the JPEG2000 bitstream, in: *Communications and Multimedia Security (CMS 2003)*, Vol. 2828 of *Lecture Notes in Computer Science*, Springer, 2003, pp. 194–204. doi:[10.1007/978-3-540-45184-6\\_16](https://doi.org/10.1007/978-3-540-45184-6_16).
- [5] G. Bhatnagar, Q. M. J. Wu, Selective image encryption based on pixels of interest and singular value decomposition, *Digital Signal Processing* 22 (4) (2012) 648–663. doi:[10.1016/j.dsp.2012.02.005](https://doi.org/10.1016/j.dsp.2012.02.005).
- [6] Y. Alghamdi, A. Munir, Image encryption algorithms: A survey of design and evaluation metrics, *Journal of Cybersecurity and Privacy* 4 (1) (2024) 126–152. doi:[10.3390/jcp4010007](https://doi.org/10.3390/jcp4010007).
- [7] T. Gupta, A. Selwal, A. K. Sharma, A survey on image cryptography mechanisms: Hitherto, and future directions, *Computer Science Review* 58 (2025) 100783. doi:[10.1016/j.cosrev.2025.100783](https://doi.org/10.1016/j.cosrev.2025.100783).
- [8] S. Lian, J. Sun, Z. Wang, Security analysis of a chaos-based image encryption algorithm, *Physica A: Statistical Mechanics and its Applications* 351 (2) (2005) 645–661. doi:[10.1016/j.physa.2005.01.001](https://doi.org/10.1016/j.physa.2005.01.001).
- [9] R. Rhouma, E. Solak, S. Belghith, Cryptanalysis of a new substitution–diffusion based image cipher, *Communications in Nonlinear Science and Numerical Simulation* 15 (7) (2010) 1887–1892. doi:[10.1016/j.cnsns.2009.07.007](https://doi.org/10.1016/j.cnsns.2009.07.007).

- [10] C. Çokal, E. Solak, Cryptanalysis of a chaos-based image encryption algorithm, *Physics Letters A* 373 (15) (2009) 1357–1360. doi:[10.1016/j.physleta.2009.02.030](https://doi.org/10.1016/j.physleta.2009.02.030).
- [11] Y. Liu, L. Y. Zhang, J. Wang, Y. Zhang, K.-W. Wong, Chosen-plaintext attack of an image encryption scheme based on modified permutation–diffusion structure, *Nonlinear Dynamics* 84 (4) (2016) 2241–2250. doi:[10.1007/s11071-016-2642-3](https://doi.org/10.1007/s11071-016-2642-3).
- [12] S. Dhall, S. K. Pal, K. Sharma, Cryptanalysis of image encryption scheme based on a new 1d chaotic system, *Signal Processing* 146 (2018) 22–32. doi:[10.1016/j.sigpro.2017.12.021](https://doi.org/10.1016/j.sigpro.2017.12.021).
- [13] B. Norouzi, S. Mirzakuchaki, Breaking an image encryption algorithm based on the new substitution stage with chaotic functions, *Optik* 127 (14) (2016) 5695–5701. doi:[10.1016/j.ijleo.2016.03.076](https://doi.org/10.1016/j.ijleo.2016.03.076).
- [14] S. Dhall, K. Yadav, Cryptanalysis of substitution-permutation network based image encryption schemes: A systematic review, *Nonlinear Dynamics* 112 (17) (2024) 14719–14744. doi:[10.1007/s11071-024-09816-0](https://doi.org/10.1007/s11071-024-09816-0).
- [15] M. SaberiKamarposhti, A. Ghorbani, M. Yadollahi, A comprehensive survey on image encryption: Taxonomy, challenges, and future directions, *Chaos, Solitons & Fractals* 178 (2024) 114361. doi:[10.1016/j.chaos.2023.114361](https://doi.org/10.1016/j.chaos.2023.114361).
- [16] A. Benamira, D. Gérard, T. Peyrin, Q. Q. Tan, A deeper look at machine learning-based cryptanalysis, in: *Advances in Cryptology – EUROCRYPT 2021*, Vol. 12696 of *Lecture Notes in Computer Science*, Springer, 2021, pp. 805–835. doi:[10.1007/978-3-030-77870-5\\_28](https://doi.org/10.1007/978-3-030-77870-5_28).
- [17] H. Krawczyk, Cryptographic extraction and key derivation: The HKDF scheme, in: *Advances in Cryptology – CRYPTO 2010*, Vol. 6223 of *Lecture Notes in Computer Science*, Springer, 2010, pp. 631–648. doi:[10.1007/978-3-642-14623-7\\_34](https://doi.org/10.1007/978-3-642-14623-7_34).
- [18] L. Chen, Recommendation for key derivation using pseudorandom functions, NIST Special Publication SP 800-108 Rev. 1 (Upd. 1), National Institute of Standards and Technology (2024). doi:[10.6028/NIST.SP.800-108r1-upd1](https://doi.org/10.6028/NIST.SP.800-108r1-upd1).

- [19] A. Gohr, Improving attacks on round-reduced Speck32/64 using deep learning, in: *Advances in Cryptology – CRYPTO 2019*, Vol. 11693 of *Lecture Notes in Computer Science*, Springer, 2019, pp. 150–179. [doi:10.1007/978-3-030-26951-7\\_6](https://doi.org/10.1007/978-3-030-26951-7_6).
- [20] Y. Huang, L. Li, Y. Guo, Y. Ou, X. Huang, An efficient differential analysis method based on deep learning, *Computer Networks* 224 (2023) 109622. [doi:10.1016/j.comnet.2023.109622](https://doi.org/10.1016/j.comnet.2023.109622).
- [21] X. Zhang, J. Wu, H. Guo, M. Li, W. Zhang, Remote-sensing image encryption algorithm using the advanced encryption standard, *Applied Sciences* 8 (9) (2018) 1540. [doi:10.3390/app8091540](https://doi.org/10.3390/app8091540).
- [22] S. Zhu, C. Zhu, W. Wang, A new image encryption algorithm based on chaos and secure hash SHA-256, *Entropy* 20 (9) (2018) 716. [doi:10.3390/e20090716](https://doi.org/10.3390/e20090716).
- [23] Y. Bentoutou, E. Bensikaddour, N. Taleb, N. Bounoua, An improved image encryption algorithm for satellite applications, *Advances in Space Research* 66 (1) (2020) 176–193. [doi:10.1016/j.asr.2019.09.027](https://doi.org/10.1016/j.asr.2019.09.027).
- [24] F. T. Muhaya, Chaotic and AES cryptosystem for satellite imagery, *Telecommunication Systems* 52 (2) (2013) 573–581. [doi:10.1007/s11235-011-9462-z](https://doi.org/10.1007/s11235-011-9462-z).
- [25] J. Fridrich, Symmetric ciphers based on two-dimensional chaotic maps, *International Journal of Bifurcation and Chaos* 8 (6) (1998) 1259–1284. [doi:10.1142/S021812749800098X](https://doi.org/10.1142/S021812749800098X).
- [26] H. Wen, Y. Lin, L. Yang, R. Chen, Cryptanalysis of an image encryption scheme using variant hill cipher and chaos, *Expert Systems with Applications* 250 (2024) 123748. [doi:10.1016/j.eswa.2024.123748](https://doi.org/10.1016/j.eswa.2024.123748).
- [27] H. Wen, Y. Lin, Cryptanalysis of an image encryption algorithm using quantum chaotic map and DNA coding, *Expert Systems with Applications* 237 (2024) 121514. [doi:10.1016/j.eswa.2023.121514](https://doi.org/10.1016/j.eswa.2023.121514).
- [28] L. D. Singh, R. Thingbaijam, R. Patgiri, K. M. Singh, Cryptanalysis of cross-coupled chaotic maps multi-image encryption scheme, *Journal of Information Security and Applications* 80 (2024) 103694. [doi:10.1016/j.jisa.2023.103694](https://doi.org/10.1016/j.jisa.2023.103694).

- [29] C. E. Shannon, A mathematical theory of communication, *The Bell System Technical Journal* 27 (3) (1948) 379–423. [doi:10.1002/j.1538-7305.1948.tb01338.x](https://doi.org/10.1002/j.1538-7305.1948.tb01338.x).
- [30] S. Goldwasser, S. Micali, Probabilistic encryption, *Journal of Computer and System Sciences* 28 (2) (1984) 270–299. [doi:10.1016/0022-0000\(84\)90070-9](https://doi.org/10.1016/0022-0000(84)90070-9).
- [31] G. Wang, X. Ye, B. Zhao, A novel remote sensing image encryption scheme based on block period arnold scrambling, *Nonlinear Dynamics* 112 (19) (2024) 17477–17507. [doi:10.1007/s11071-024-09953-6](https://doi.org/10.1007/s11071-024-09953-6).
- [32] J. Tang, X. Jiang, C. Huang, C. Ding, M. Deng, Z. Huang, Texture-adaptive hierarchical encryption method for large-scale HR remote sensing image data, *Remote Sensing* 17 (17) (2025) 2940. [doi:10.3390/rs17172940](https://doi.org/10.3390/rs17172940).